

Discovery of Dual-Functional Amorphous Titanium Suboxide to Promote Polysulfide Adsorption and Regulate Sulfide Growth in Li–S Batteries

Donghee Gueon, Jisu Yoon, Jinhwan Cho, and Jun Hyuk Moon*

Lithium-sulfur (Li–S) batteries are promising as next-generation energy storage systems. Adsorbents for sulfide species are favorably applied to the cathode, but this substrate often results in a surface-passivating lithium sulfide (Li_2S) film with a strong adsorption of Li_2S . Here, an amorphous titanium suboxide (a-TiO_x) is presented that strongly adsorbs lithium polysulfides (Li_2S_x , $x < 6$) but relatively weakly adsorbs to Li_2S . With these characteristics, the a-TiO_x achieves high conversion of Li_2S_x and high sulfur utilization accompanying the growth of particulate Li_2S . The DFT calculations present a mechanism for particulate growth driven by the promoted diffusion and favorable clustering of Li_2S . The a-TiO_x -coated carbon nanotube-assembled film (CNTF) cathode substrate cell achieves a high discharge capacity equivalent to 90% sulfur utilization at 0.2 C. The cell also delivers a high capacity of 850 mAh g^{-1} even at the ultra-high-speed of 10 C and also exhibits high stability of capacity loss of 0.0226% per cycle up to 500 cycles. The a-TiO_x /CNTF is stacked to achieve a high loading of 7.5 mg S cm^{-2} , achieving a practical areal capacity of 10.1 mAh cm^{-2} .

batteries due to their high theoretical capacity.^[1] A relatively low density of sulfur is advantageous for lightweight or high specific energy devices.^[2] Moreover, the active material sulfur is inexpensive and environmentally friendly.^[3] However, at present, the high theoretical capacity of Li-S batteries has not been sufficiently achieved. The main reason is that the sulfur conversion to form lithium sulfide, Li_2S via an intermediate of lithium polysulfides (LiPSs) takes place in multiple phases.^[4] Specifically, the conversion from electrolyte-soluble LiPSs to insoluble Li_2S upon discharge is sluggish with a high energy barrier due to a large decrease in system entropy.^[5,6] Moreover, the growth of Li_2S by electrochemical reduction on the cathode substrate is uncontrollable, often resulting in ionically/electrically passivating the substrate to inhibit full utilization of sulfur.^[7,8]

Much effort has been devoted to introducing advanced materials as cathode substrates.^[9,10] The metal compound traps LiPSs with high chemical affinity and also serves as a mediator to promote the conversion of LiPSs.^[11] Oxides have been widely applied because of their facile synthesis into various morphologies and high surface polarity.^[12,13] The oxide also chemically immobilizes LiPSs by thiosulfate-polythionate conversion.^[14] In addition to oxides, sulfides, nitrides, and phosphides have been demonstrated due to their high electrical conductivity as well as their polar surfaces.^[15–19] Recently, metal compound composites have been introduced to regulate multi-step sulfur conversion.^[20,21] For example, the composite substrate of MoS_2 and MoN has been introduced to enhance the adsorption and conversion of LiPSs, respectively.^[20] The composites of iron phthalocyanine and octafluoronaphthalene have been introduced into cathode substrates to facilitate the conversion of higher and lower-order LiPSs, respectively.^[21] They have been particularly successful in achieving cell stability by promoting the adsorption/conversion of LiPSs. However, the cathode substrate, which also controls the growth of Li_2S , remains a challenge.

The control of Li_2S growth has rather been achieved by controlling the donicity of the electrolyte. This approach prevented the passivation of the electrode surface by the growth of Li_2S , thus achieving high sulfur utilization.^[22,23] Specifically, a high donicity electrolyte such as dimethyl sulfoxide (DMSO) induced partial solvation of Li_2S , thereby inhibiting the film-like growth

1. Introduction

Lithium-sulfur (Li–S) batteries are attracting attention as a next-generation energy storage system to replace lithium-ion

D. Gueon, J. Yoon, J. H. Moon
Department of Chemical and Biomolecular Engineering
Institute of Emergent Materials
Sogang University
Baekbeom-ro 35, Mapo-gu, Seoul 04107, Republic of Korea
E-mail: junhyuk@sogang.ac.kr

J. Cho
Department of Chemical and Biological Engineering
Korea University
145 Anam-ro, Seongbuk-gu, Seoul 02841, Republic of Korea

J. Cho
KU-KIST Graduate School of Converging Science and Technology Korea University
145 Anam-ro, Seongbuk-gu, Seoul 02841, Republic of Korea

 The ORCID identification number(s) for the author(s) of this article can be found under <https://doi.org/10.1002/advs.202200958>

© 2022 The Authors. Advanced Science published by Wiley-VCH GmbH. This is an open access article under the terms of the Creative Commons Attribution License, which permits use, distribution and reproduction in any medium, provided the original work is properly cited.

DOI: 10.1002/advs.202200958

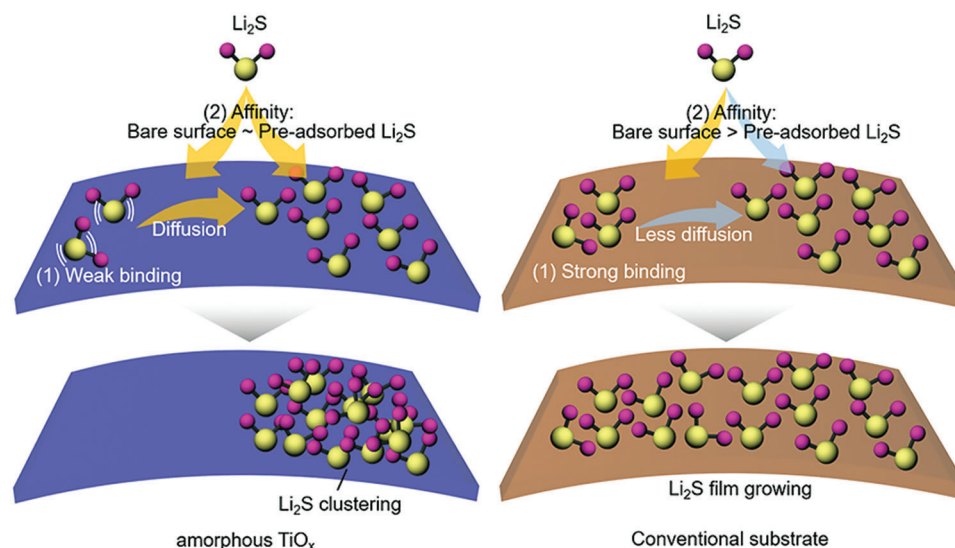


Figure 1. Scheme depicting the growth mechanism of particulate Li_2S on a- TiO_x substrate. (Left) On the a- TiO_x , the affinity for Li_2S is relatively weak, and the affinity between the bare surface and the adsorbed Li_2S surface is similar. This case favors the particulate growth of Li_2S by diffusion and clustering of Li_2S . (Right) TiO_2 has a strong affinity for Li_2S , and this affinity is stronger than the surface on which Li_2S is adsorbed. This induces a film-like growth of Li_2S on the surface.

of Li_2S .^[22,23] This effect has also been demonstrated in electrolytes containing high donicity salts such as lithium bromide and lithium nitrate.^[23] Recently, the application of 1,3-dimethyl-2-imidazolidinone (DMI) has been confirmed to promote the formation of particulate Li_2S by activating the pathway to generate Li_2S via sulfide radicals.^[24] This result exhibited a high discharge capacity of 1595 mAh g^{-1} , corresponding to 95% sulfur utilization. Despite these achievements, the reforming of the electrolyte still has to resolve issues such as corrosion of Li anodes and interactions with metal compound substrates.^[24,25] Therefore, there is still great demand for a substrate capable of controlling Li_2S growth for the complete and reversible utilization of sulfur.

To tackle this issue, we explored an amorphous titanium suboxide layer-coated substrate as a cathode substrate. Amorphous metal oxides have been widely applied as catalysts due to their high activity originating from abundant defective sites.^[26–31] In addition, in Li-S cell application, the amorphous metal oxide showed strong adsorption to LiPS molecules. Metal compound-coated substrates that exhibit strong interactions with LiPSs often exhibit a strong affinity for Li_2S as well. Cui and co-workers found that the affinity for sulfide species on polar substrates consisted of chemical bonding and van der Waals forces and estimated a stronger affinity for Li_2S than long-chain LiPSs by strong chemical bonding. Wang and co-workers have confirmed that the NiMoO_4 surface, which has a strong affinity with LiPSs, exhibits strong binding energy to Li_2S .^[32,33] We presume that on such a substrate, Li_2S is less diffusive and the film-like Li_2S overlying the substrate grows (see Figure 1). A substrate with a strong affinity for LiPSs but a weak affinity for Li_2S can induce the growth of Li_2S particles.

We confirm by DFT calculation that the amorphous titanium suboxide (a- TiO_x) surface exhibits relatively weak binding to Li_2S despite strong binding to LiPSs; on the TiO_2 surface for comparison, the stronger binding energy is calculated for Li_2S than for LiPSs under the same conditions (see Figure 1). Moreover, on the

a- TiO_x surface, the affinity for Li_2S is similar between the Li_2S -adsorbed surface and the bare surface; TiO_2 has a strong affinity for bare surfaces. These results present favorable clustering for Li_2S on a- TiO_x and growth of Li_2S covering the bare surface of TiO_2 . We confirm the high discharge capacity is accompanying the growth of particulate Li_2S on a- TiO_x by chronoamperometry; film-like Li_2S is observed on TiO_2 . With the strong adsorption of LiPSs and also the regulation of Li_2S growth, a- TiO_x -containing cathode Li-S batteries achieve high sulfur utilization. We achieve high sulfur utilization of up to 90% at 0.2 C. At the ultra-high rate of 10 C, a high specific capacity of 850 mAh g^{-1} with a capacity loss of 0.084% per cycle up to 200 cycles is achieved. At a high sulfur load of 7.5 mg S cm^{-2} , a practical areal capacity of 10.1 mAh cm^{-2} is also achieved.

2. Results and Discussion

2.1. Fabrication of a- TiO_x /CNTF

We obtain a- TiO_x by thermal evaporation from a source of titanium monoxide (TiO). Previously, titanium suboxide was often obtained by catalytic reduction of crystalline TiO_2 in a high-temperature hydrogen atmosphere.^[34–36] Compared to this process, thermal evaporation facilitates the preparation of titanium suboxide (see Figure S1, Supporting Information). a- TiO_x is coated on the CNT-assembled film (CNTF) and applied as a cathode substrate, as described in Figure 2a. The a- TiO_x is mainly coated on the top region of the CNTF because of the directional deposition in a high vacuum (Figure 2b, and S2, Supporting Information). Due to the porous structure of CNTF, a- TiO_x is coated on several layers of CNTs on the surface (Figure 2c).

The a- TiO_x layer consists of particles with sizes on the order of 100 nm (Figure 2d and Figure S2, Supporting Information). The HR-TEM images and SAED patterns of a- TiO_x reveal an amorphous structure that does not exhibit long-range order

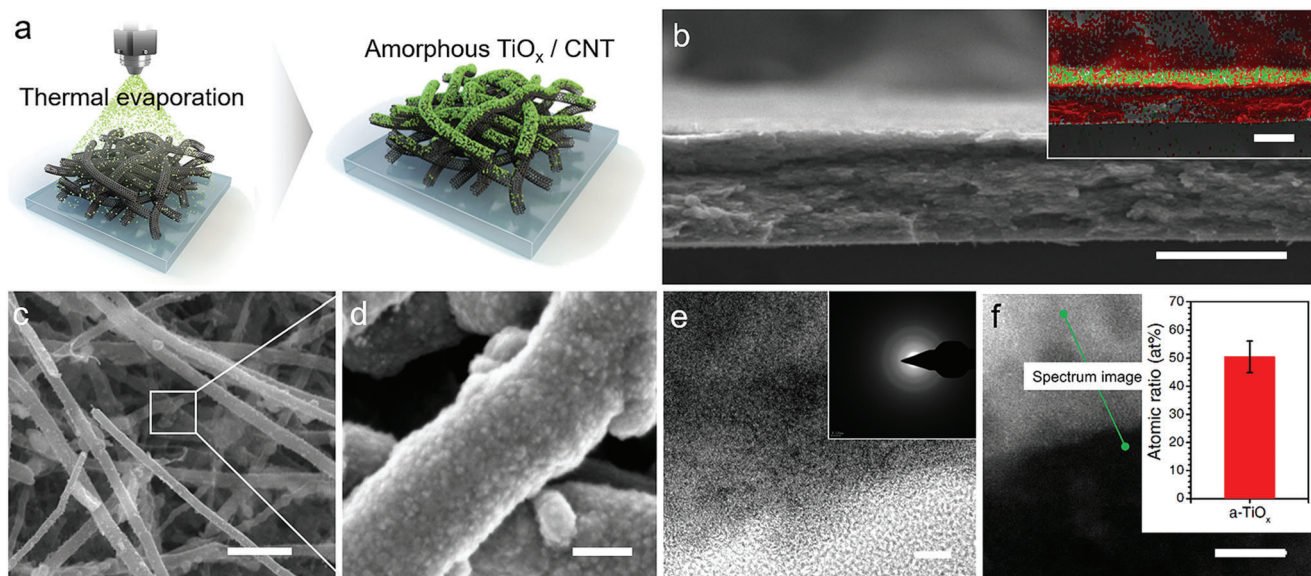


Figure 2. a) Schematic diagram of a-TiO_x/CNTF production. b) Cross-sectional SEM image of a-TiO_x/CNTF (scale bar: 100 μm) and its elemental mapping image (inset image, scale bar: 100 μm). c) Low and d) high magnification SEM images of a-TiO_x/CNTF (scale bar: 100 μm for c, 100 nm for d). e) High-resolution TEM image of a-TiO_x and electron diffraction image of the selected area of a-TiO_x (scale bar: 5 nm). f) HAADF-STEM image of a-TiO_x with a profiling line. The inset is the atomic ratio of Ti/O by EELS.

(Figure 2e). During the thermal deposition, the temperature of the CNTF substrate is maintained at room temperature to achieve rapid thermal quenching, whereby an amorphous phase is obtained.

A high-angle annular dark-field scanning transmission electron microscope (HAADF-STEM) image (Drift-corrected) of a-TiO_x with a profiling line is displayed in Figure 2f. The inset shows the atomic ratio of Ti and O by electron energy loss spectroscopy (EELS). The EELS analysis confirms that the O/Ti ratio in a-TiO_x ranges from 0.8 to 1.2. We determine that a-TiO_x has the composition of TiO. In the phase diagram for the Ti/O ratio, it is confirmed that monoclinic TiO exists as an independent phase at the ratio ≈1.^[37,38]

2.2. Exploring Lithium Polysulfide Adsorption and Lithium Sulfide Growth on a-TiO_x

First, we analyze the adsorption of LiPS on a-TiO_x/CNTF. For comparison, TiO₂-coated CNTF (TiO₂/CNTF) is prepared. The TiO₂/CNTF sample is obtained by annealing a-TiO_x/CNTF at 480 °C in an air atmosphere (Note S1, Supporting Information); this temperature is inert to CNTF. The preparation of the control sample by this process minimizes the morphological difference from the a-TiO_x/CNTF sample. The XRD and Raman spectra of the TiO₂/CNTF confirm crystalline TiO₂ (Figure S3, Supporting Information).

The inset shows digital camera images of a-TiO_x/CNTF and TiO₂/CNTF samples after 3 h adsorption immersed in an electrolyte containing Li₂S₄. Compared to the TiO₂ sample, the a-TiO_x sample shows an almost transparent solution (Figure 3a). In Figure 3a, the UV-vis spectra of the electrolyte solutions of each sample after the adsorption are compared; the peak at 421 nm

is attributed to the absorption by Li₂S₄.^[39] The absorption peak of a-TiO_x/CNTF is significantly lower than that of TiO₂/CNTF. The a-TiO_x substrate has a higher adsorption capacity for Li₂S₄ compared to TiO₂.

The strong affinity of a-TiO_x for LiPSs can be attributed to the strong Lewis acid-base interaction due to the vacant d-orbitals of a-TiO_x.^[40,41] We evaluate the affinity by DFT-based binding energy calculations. The binding energy is obtained by $E_{\text{total}} - E_{\text{ads}} - E_{\text{surf}}$, where E_{total} is the total energy of the absorbed system, E_{ads} is the energy of the optimized Li₂S₄ in a vacuum, and E_{surf} is the energy of the optimized bare surface.^[42] As an atomic model for a-TiO_x, amorphous titanium monoxide (TiO) is constructed using the melt quenching technique.^[43,44] Specifically, a crystalline model obtained using ab initio molecular dynamics (AIMD) was diffused at 6000 K and then quenched at 300 K.^[45,46] This melting and quenching technique through AIMD has been previously applied to construct an amorphous interface of Sb₂Te₃. In Figure 3b, the binding energies of Li₂S₄ on carbon, TiO₂, and a-TiO_x are compared. The carbon surface exhibits weak adsorption to Li₂S₄, with a binding energy of only -0.6 eV. The binding energy on the a-TiO_x surface is 56% higher than that on TiO₂. We also analyze the average distance between the S atoms and the atoms on the substrate surface, confirming that the interatomic distance is 85% shorter on a-TiO_x than on TiO₂. These results indicate stronger bonding of Li₂S₄ on a-TiO_x and correspond well with the results of adsorption experiments.

Second, we compare the kinetics of sulfur conversion on both substrates. Through DFT calculations, we compare the Gibbs free energy profiles for the discharge process on the two substrates (Figure 3c and see Figure S4, Supporting Information). Both substrates exhibit spontaneous exothermic reactions in the process of sulfur to Li₂S₂. However, an energy barrier is observed in the formation of Li₂S, which has been reported as a

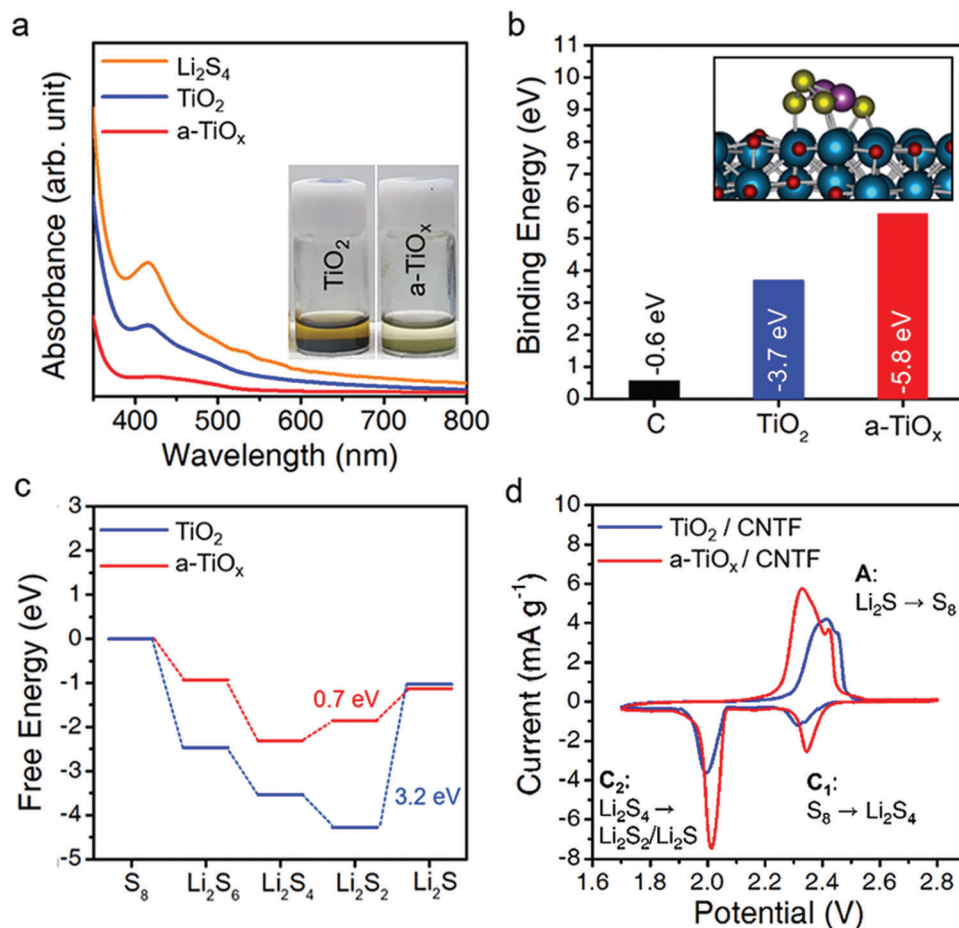


Figure 3. a) UV-vis spectra of electrolytes containing Li₂S₄, and UV-vis spectra of Li₂S₄ electrolytes after 4 h immersion of a-TiO_x/CNTF and TiO₂/CNTF. Inset is a digital camera image of an electrolyte containing a-TiO_x/CNTF and TiO₂/CNTF, respectively. b) Binding energy of Li₂S₄ on carbon, TiO₂, and a-TiO_x, respectively, by DFT calculation. Inset is an energy-optimized atomic configuration image of Li₂S₄ adsorbed on a-TiO_x. Titanium monoxide (TiO) is applied as an atomic model for TiO_x. c) The individual free energy profiles for the discharge process on a-TiO_x and TiO₂. d) Cyclic voltammetry curves for a-TiO_x/CNTF and TiO₂/CNTF electrodes at a scan rate of 0.1 mV s⁻¹.

rate-determining step.^[47,48] Compared to TiO₂, the a-TiO_x substrate exhibits much lower barrier energy. The barrier energies for a-TiO_x and TiO₂ are 0.7 and 3.2 eV, respectively. This result indicates a higher rate of sulfur conversion on the a-TiO_x substrate.

Compared with TiO₂, the enhanced sulfur conversion of a-TiO_x is also confirmed by the response of the reaction peak in the cyclic voltammetry. Figure 3d shows CV curves for a-TiO_x/CNTF and TiO₂/CNTF cathode substrates in LiPS-containing electrolytes. The current profile shows two reduction peaks and one oxidation peak. Each reduction peak represents the conversion of elemental sulfur to higher LiPSs (Li₂S_x, x = 4, 6) and lower LiPSs (Li₂S_x, x = 1, 2), respectively.^[49] The oxidation sweep shows one peak corresponding to the conversion of lower LiPSs to sulfur. Compared with the TiO₂/CNTF, the a-TiO_x/CNTF shows a higher current at a higher voltage for both reduction peaks and a clearer current peak in the oxidation sweep.^[16,50] This clearly indicates a faster sulfur conversion reaction on the a-TiO_x surface.

In the CV analysis, the a-TiO_x substrate shows excellent kinetics for the sluggish formation of Li₂S during discharge. We analyze the capacity for Li₂S₄ to Li₂S conversion and the morphol-

ogy of Li₂S through chronoamperometry. The measurement is achieved by applying a voltage of 2.05 V to the TiO₂/CNTF or a-TiO_x/CNTF substrate in an electrolyte containing Li₂S₄. The discharge profile and the growth morphology of Li₂S after discharge on each substrate are presented in Figures 4a,b, respectively. The a-TiO_x/CNTF cathode cell shows a longer discharge time than the TiO₂/CNTF cell. The calculated capacity based on the integral area of the discharge curve is 129 mAh g⁻¹ for the a-TiO_x/CNTF, which is 53% larger than that of the TiO₂/CNTF. For the bare CNTF electrode, only a capacity of 62 mAh g⁻¹ was obtained. (see Note S2, Supporting Information)

Note that the formation of particulate Li₂S is observed on the a-TiO_x/CNTF surface (Figure 4b, see also Note S2, Supporting Information). It has been reported that such morphological growth does not impede the transport of lithium ions/charges, resulting in high sulfur utilization.^[51,52] The high capacity for Li₂S₄-to-Li₂S conversion in a-TiO_x/CNTF is attributed to this particle growth. In contrast, the TiO₂/CNTF sample exhibits film-like growth of Li₂S, which results in poor sulfur utilization. (see Figure S6, Supporting Information). Note the growth of particulate Li₂S despite the strong adsorption of a-TiO_x to LiPS. On a substrate with

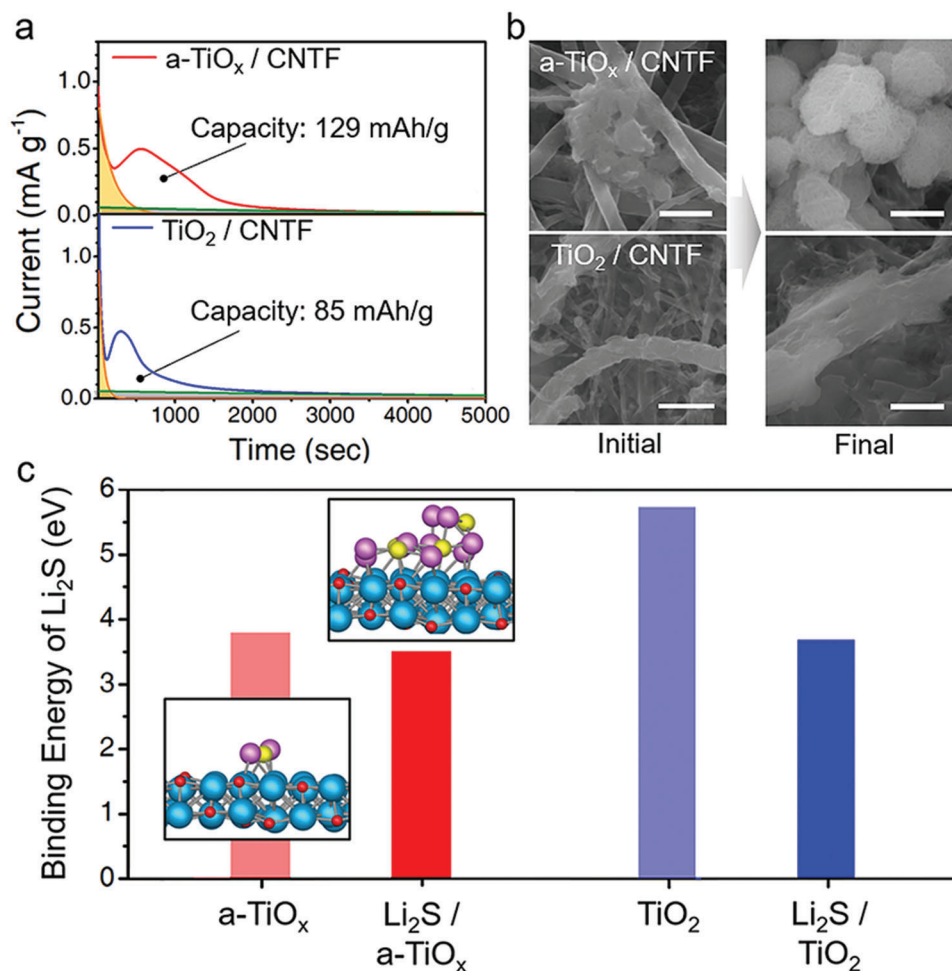


Figure 4. a) Potentiostatic discharge (0.5 M Li_2S_6 , 2.05 V) curves forming Li_2S in a- TiO_x/CNTF and TiO_2/CNTF cathodes. b) SEM images of Li_2S grown on a- TiO_x and TiO_2 layers of a- TiO_x/CNTF and TiO_2/CNTF cathode substrates, respectively, at the beginning of discharge and after full discharge. (scale bar: 500 nm) c) Binding energy for adsorption of Li_2S on a- TiO_x and TiO_2 surfaces, respectively. Binding energy to adsorb Li_2S to each surface on which four Li_2S molecules have been pre-adsorbed. Titanium monoxide (TiO) is applied as an atomic model for TiO_x .

strong adsorption capacity, abundant LiPSs are present on the surface, which facilitates the growth of the film-like Li_2S with rapid nucleation-growth; Nazar and co-workers have observed the formation of Li_2S films by adsorption of LiPS molecules and surface-mediated reduction on metallic polar Ti_4O_7 .^[53]

To analyze the particulate growth on the a- TiO_x surface, the binding energy for Li_2S on the TiO_2 and a- TiO_x surfaces is compared by DFT calculation. a- TiO_x shows weak binding corresponding to only 66% of the binding energy on TiO_2 , as shown in Figure 4c. This implies that the reduced Li_2S molecules diffuse easily on the a- TiO_x substrate, as depicted in Figure 1. Previously, Kim and co-workers have reported the growth of particulate Li_2S by diffusion of partially dissolved Li_2S and also clustering of Li_2S .^[52] Moreover, on each substrate, we calculate the binding energy of Li_2S on the bare surface and on the surface on which Li_2S is pre-adsorbed (see Figure 4c). The TiO_2 surface exhibits stronger binding energy on the bare surface than the Li_2S -adsorbed surface. This reveals that the growth covering the bare surface, i.e., a film-like growth, is thermodynamically favorable on the TiO_2 surface. In contrast, for the a- TiO_x , the binding ener-

gies on both surfaces are similar. That is, the clustering of Li_2S is more favorable on the surface of a- TiO_x than on TiO_2 , as depicted in Figure 1. Considering the effect of the electrolyte solvent to stabilize the sulfide, the clustering between Li_2S can be further promoted by a similar action to the hydrophobic interaction.^[52–54] Briefly, the DFT calculations reveal favorable surface diffusion of Li_2S and also clustering between Li_2S on a- TiO_x , supporting the particulate growth observed on a- TiO_x substrates.

2.3. Electrochemical Performance of a- TiO_x/CNTF Cells

We prepare a Li-S battery containing a cathode substrate of sulfur-loaded a- TiO_x/CNTF . The areal loading mass of sulfur is typically 1 mg cm^{-2} (Figure S6, Supporting Information). The charge-discharge profile of a- TiO_x/CNTF cell at 0.2 C is shown in Figure 5a. The a- TiO_x/CNTF cell delivers a capacity of 1502 mAh g^{-1} , corresponding to $\approx 90\%$ sulfur utilization. This sulfur utilization is superior to recent results for metal compound/carbon cathode substrate cells (Table S1, Supporting Information) and is

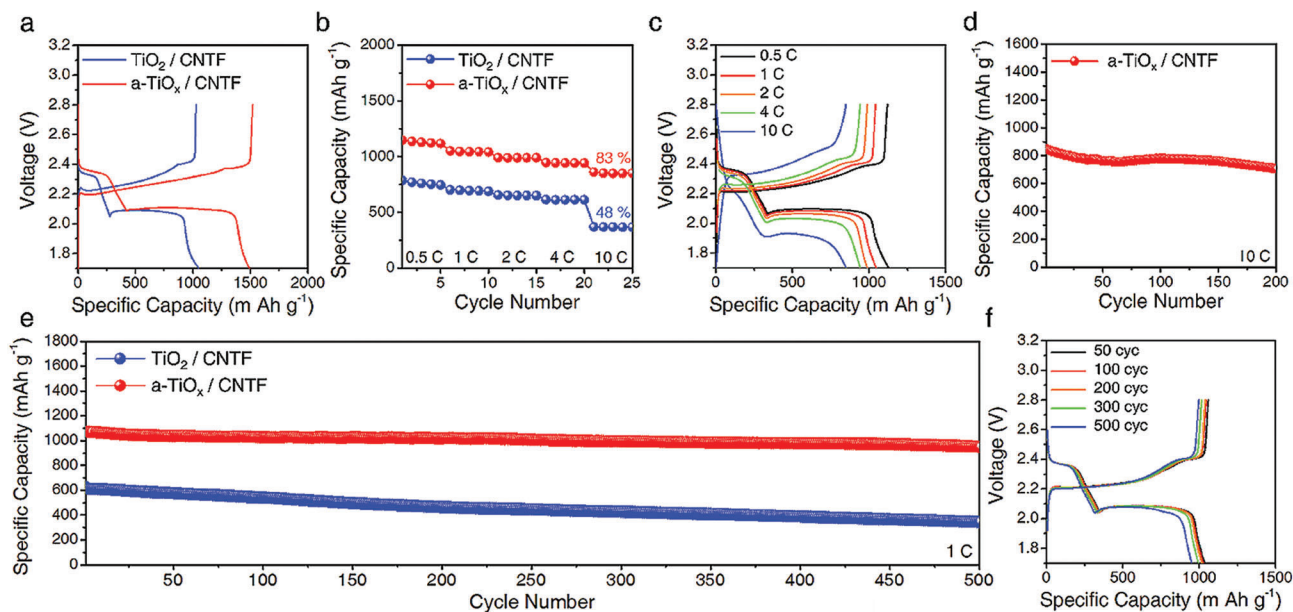


Figure 5. a) Voltage profiles of TiO₂/CNTF and a-TiO_x/CNTF cathode cells at 0.2 C. b) Discharge capacity of TiO₂/CNTF and a-TiO_x/CNTF cathode cells at various current densities from 0.5 C to 10 C. c) Voltage profiles of a-TiO_x/CNTF cathode cells at various current densities from 0.5 C to 10 C. d) Cycling performance for a-TiO_x/CNTF cathode cells at 10 C. e) Cycling performance for TiO₂/CNTF and a-TiO_x/CNTF cathode cells at 1 C. f) Voltage profiles of a-TiO_x/CNTF cathode cells at 1 C.

comparable to the values achieved with controlled growth of Li₂S in high donicity electrolytes.^[23,24,52,55] The discharge capacity of the TiO₂/CNTF cell is 1050 mAh g⁻¹, which is only 70% of the capacity of the a-TiO_x/CNTF cell.

The discharge capacities of a-TiO_x/CNTF and TiO₂/CNTF cells are recorded with a 20-fold increase in the C-rate from 0.5 C to an ultrafast rate of 10 C (Figure 5b). The capacity of the a-TiO_x/CNTF cell at 10 C exhibits high retention of 83% of the capacity at 0.5 C, whereas the retention of the TiO₂/CNTF cell is only 48%. The capacity at 10 C of the a-TiO_x/CNTF cell, 850 mAh g⁻¹, is superior to the previous results highlighting the high capacity at a high rate (Figure S7, Supporting Information). In Figure 5c, the discharge-charge profile of the a-TiO_x/CNTF cell shows two stable plateaus revealing a reversible sulfur redox reaction even at a high current density of 10 C-rate. In addition, the a-TiO_x/CNTF cell exhibits a reversible charge/discharge cycle even at 10 C, as shown in Figure 5d. At 200 charge/discharge cycles, the specific capacity is 707 mAh g⁻¹, maintaining 83% of the initial capacity. The a-TiO_x/CNTF cell shows a stable voltage profile up to 200 cycles even at a current density of 10 C (Figures S8 and S9, Supporting Information).

The cyclic stability of a-TiO_x/CNTF cells is evaluated at 1 C, as shown in Figure 5e. During 500 cycles, the a-TiO_x/CNTF cell exhibits high stability with a capacity loss of 0.0226% per cycle; the TiO₂/CNTF cell shows a capacity loss per cycle four times greater. The discharge/charge profile in Figure 5f shows a stable profile for up to 500 cycles (see Figure S9, Supporting Information). The a-TiO_x/CNTF cathode cell achieves high reversible capacity, especially at high rates. This is due to the controlled growth of Li₂S as well as the continuous and complete conversion of LiPSs to Li₂S on a-TiO_x/CNTF substrates; We confirm the formation of particulate Li₂S observed in the chronoamperometry also in constant current discharge (Figure S10, Supporting Information).

The high areal capacity that requires high sulfur loading cathodes is a crucial metric for practical applications of Li-S batteries.^[56] We stacked three a-TiO_x/CNTFs to obtain a high sulfur loading electrode of 7.5 mg cm⁻². The cross-sectional SEM, shown in Figure 6a, shows a film composed of three layers of a-TiO_x/CNTF. The operando EIS analysis of this multilayer a-TiO_x/CNTF cathode substrate cell shows low interfacial resistance between layers and also reversible sulfur-Li₂S conversion over this substrate maintained during charge/discharge (Figure S11, Supporting Information). We also confirm the growth of particulate Li₂S in the multilayer a-TiO_x/CNTF; The SEM image shown in Figure 6b shows particulate Li₂S in the a-TiO_x-coated region at full discharge. The areal capacity of the multilayer a-TiO_x/CNTF cell evaluated at 0.5 C delivers 10.1 mAh cm⁻² at initial discharge and 8.5 mAh cm⁻² at 70 cycles (Figure 6c and S9, Supporting Information). This value exceeds the typical areal capacity range of 2 – 4 mAh cm⁻² for conventional lithium-ion batteries.^[57,58]

The areal capacity is assessed at an increasing C-rate from 0.5 C to 2 C (Figure 6d). The multilayer a-TiO_x/CNTF cell delivers a high capacity of 4.3 mAh cm⁻² even under high current density conditions of 2 C (see Figure S12, Supporting Information). We use the Ragone plot to compare cell performance from a practical perspective of various composite substrate cells and a-TiO_x/CNTF cells. The a-TiO_x/CNTF cell achieves high energy density and power density simultaneously (Figure S13, Supporting Information).

3. Conclusion

A cathode substrate that regulates the multiple steps of the sulfur conversion reaction is urgently needed for practical Li-S batteries. We present an a-TiO_x that strongly adsorbs LiPS and also

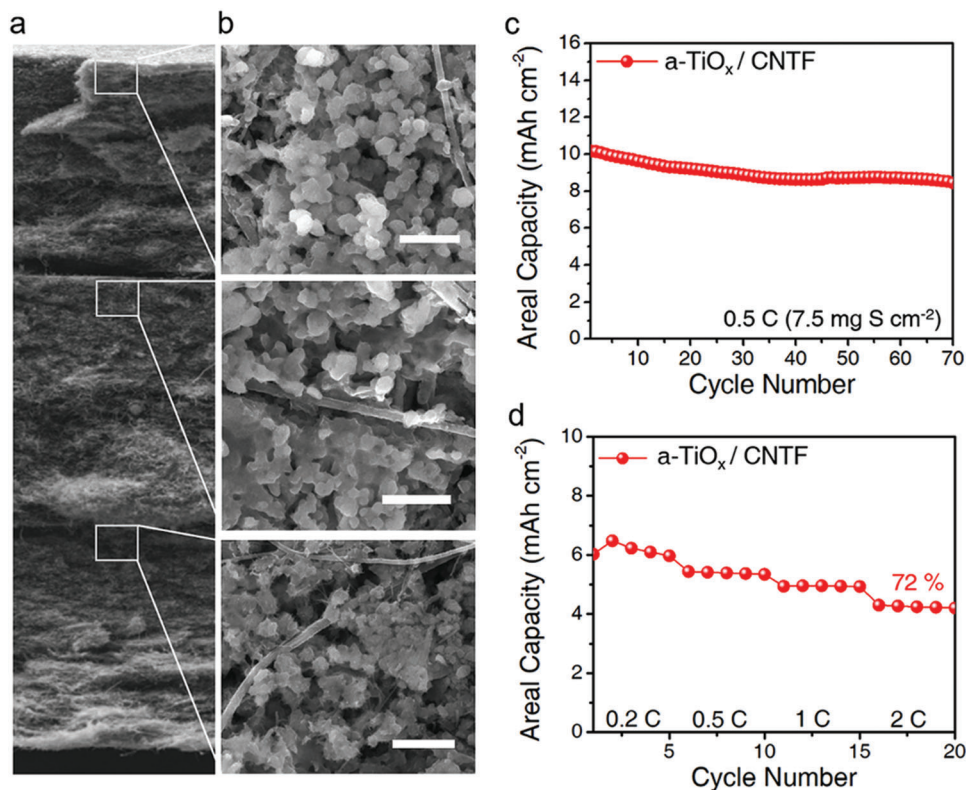


Figure 6. a) Cross-sectional SEM image of three layers of a-TiO_x/CNTF (scale bar: 50 μm). b) SEM images after full discharge in selected regions of the cathode. Particulate Li₂S is shown in the a-TiO_x coating layer of each a-TiO_x/CNTF (scale bar: 1 μm). c) Cycling performance for a-TiO_x/CNTF particle cathodes at 0.5 C with a high sulfur loading of 7.5 mg S cm⁻². d) Discharge capacities of a-TiO_x/CNTF cathode cells at various current densities of 0.2 C–2 C. (Sulfur loading: 5 mg S cm⁻²).

controls the growth of Li₂S. We prepare a-TiO_x by thermal evaporation and apply an a-TiO_x-coated CNTF as a cathode substrate. First, the a-TiO_x shows a high adsorption capacity for LiPS, which is also confirmed by the binding energy obtained by the DFT calculation. Compared to TiO₂, the a-TiO_x substrate shows an ≈56% improvement in the adsorption amount of LiPS. In addition, the a-TiO_x/CNTF substrate exhibits excellent kinetics for sulfur conversion. In the CV measurements, the a-TiO_x/CNTF shows a reduction current that is twice that of TiO₂ for the sluggish reaction of LiPS-to-Li₂S. We confirm that the excellent kinetics in a-TiO_x/CNTF is related to the growth of particulate Li₂S on the a-TiO_x layer surface. On the TiO₂, a film-like Li₂S is formed in contrast. We confirm that the formation of particulate Li₂S on a-TiO_x despite its high adsorption capacity for LiPS is due to the relatively weak affinity for Li₂S on a-TiO_x. In addition, the DFT calculation confirms that the binding energy for Li₂S on the Li₂S-adsorbed a-TiO_x surface and the bare a-TiO_x surface is similar. Through these results, we present that thermodynamically favorable diffusion and clustering of Li₂S induces the growth of particulate Li₂S on the a-TiO_x substrate. Due to this dual function of a-TiO_x in sulfur conversion, the a-TiO_x/CNTF cathode-based Li-S battery achieves high sulfur utilization of 90%. The a-TiO_x/CNTF cathode cell also exhibits high stability even at an ultra-high rate of 10 C with a discharge capacity of 850 mAh g⁻¹ and a capacity reduction of 0.0226% per cycle up to 500 cycles. High sulfur loadings for practical Li-S batteries are readily achieved by stacking

a-TiO_x/CNTFs. We achieve an areal capacity of 10.1 mAh cm⁻² in a multilayer a-TiO_x/CNTF cathode cell with a sulfur loading of 7.5 mg cm⁻²; this greatly exceeds the areal capacity of conventional Li-ion batteries. Our simple processing and high-functionality cathode substrate will speed up the practical use of Li-S batteries.

4. Experimental Section

Preparation of a-TiO_x/CNTF: CNT films were produced by vacuum filtration of multiwall CNT dispersions. a-TiO_x was coated by thermal evaporation of titanium monoxide (THIFINE, 99.9%). During the coating, the oxidation proceeds to acquire titanium suboxide (TiO_x). Thermal evaporation was performed at a pressure of 10⁻⁵ Torr, where the deposition rate was 0.5 Å s⁻¹. The substrate holder was kept at room temperature. The preparation of TiO₂/CNTF for comparison was obtained by annealing a-TiO_x/CNTF at 480 °C for 30 min in an air atmosphere.

Electrochemical Characterization: To obtain a CV curve and a galvanostatic charge/discharge profile, an electrolyte solution in which 1 M bis(trifluoromethane) sulfonimide lithium salt (LiTFSI, Sigma-Aldrich) and 0.2 M lithium nitrate (LiNO₃, Alfa Aesar) was dissolved in a 1:1 v/v% of 1,3-dioxolane (DOL, Sigma-Aldrich)/dimethylethane (DME, Sigma-Aldrich) was applied. The loading of sulfur on the cathode substrate was prepared by drop-casting sulfur-dissolved carbon disulfide. The potentiostatic discharge experiment uses a polysulfide catholyte. The catholyte was obtained by mixing sulfur and Li₂S in the electrolyte at a molar ratio of 5:1. The cell was prepared in a coin-cell type using a cathode, a Li metal (1 mm thick)

anode, and a polypropylene membrane separator (25 μm , Celgard). Cells were assembled in a controlled humidity environment (<0.3%). The ratio of electrolyte/sulfur (E/S) is 7. The low sulfur loading condition applies E/S = 15. The specific capacity was calculated based on the sulfur mass in the cathode. Cell performance was tested using a Maccor 4300 system. The test temperature was 25 $^{\circ}\text{C}$. No pre-cycling was performed. The theoretical capacity utilizes 1675 mAh g^{-1} ; the specific capacity was calculated based on the average CE value of all cell results being greater than 99%.

Calculation Details: All calculations were performed using the Quantum ESPRESSO package based on density functional theory. A generalized gradient approximation (GGA) with a Perdew-Burke-Ernzerhof (PBE) exchange-correlation function was used. A plane-wave basis set with a cut-off energy of 408 eV was applied to the calculations. The set of k-points selected by the Monkhorst-Pack scheme was used to obtain the consolidation of the Brillouin zone. For structural optimization, all ions were relaxed up to a maximum force of 0.02 eV \AA^{-1} .

Material and Structural Characterization: The surface morphology was investigated by field emission scanning electron microscopy (FE-SEM, Carl Zeiss, Supra 55 VP) and transmission electron microscopy (TEM, JEM-3010, JEOL). Elemental mapping was obtained using energy dispersive spectroscopy (EDS, BRUKER, XFlash Detector 4010). X-ray diffraction (XRD) spectra were collected on a Davinci D8 Advance diffractometer using Cu-K α radiation. (The scanning was in the range of 20 $^{\circ}$ –80 $^{\circ}$ at a scan rate of 0.05 $^{\circ}$ s $^{-1}$.) X-ray photoelectron spectroscopy (XPS) was performed using a Leybold spectrometer with an Al K α monochromatic beam (1486.6 eV) (150 W input power, ESCALAB250 XPS system, Theta Probe XPS system). Raman spectra were acquired using a Horiba Jobin Yvon LabRAM HR equipped with an air-cooled Ar-ion laser operating at 514 nm. Measurements of HAADF-STEM and EELS were performed using a spherical aberration-corrected JEM ARM-200F microscope (Cold FEG Type, JEOL) equipped with an EELS detector (965 GIF Quantum ER, GATAN). In the HAADF-STEM images, the point-to-point resolution was \approx 80 pm after Cs correction, and the angular range of the annular detector was 68–280 mrad. For the EELS, the energy dissipation was set to 0.25 eV ch^{-1} , and the full-width at half-maximum of the zero-loss peak in vacuum was 1.0 eV. The convergence and collection semi-angles were 19 and 26 mrad, respectively. Digital microscope software (GMS 3.3, GATAN) was used for image recording and processing.

Supporting Information

Supporting Information is available from the Wiley Online Library or from the author.

Acknowledgements

This work was supported by the National Research Foundation of Korea (grant no. NRF-2022R1A2C2005228, NRF-2019R1A4A1027627) and the Civil-Military Technology Cooperation Program (grant no. 19-CM-BR-03 and 20-SN-BR-03).

Conflict of Interest

The authors declare no conflict of interest.

Data Availability Statement

The data that support the findings of this study are available from the corresponding author upon reasonable request.

Keywords

amorphous titanium suboxides, DFT calculations, high sulfur loading, lithium sulfide clustering, lithium-sulfur batteries

Received: February 17, 2022

Revised: May 4, 2022

Published online:

- [1] W. Xue, Z. Shi, L. Suo, C. Wang, Z. Wang, H. Wang, K. P. So, A. Maurano, D. Yu, Y. Chen, *Nat. Energy* **2019**, *4*, 374.
- [2] A. B. Puthirath, A. Baburaj, K. Kato, D. Salpekar, N. Chakingal, Y. Cao, G. Babu, P. M. Ajayan, *Electrochim. Acta* **2019**, *306*, 489.
- [3] Y. Ansari, S. Zhang, B. Wen, F. Fan, Y. M. Chiang, *Adv. Energy Mater.* **2019**, *9*, 1802213.
- [4] Y. Song, W. Cai, L. Kong, J. Cai, Q. Zhang, J. Sun, *Adv. Energy Mater.* **2020**, *10*, 1901075.
- [5] L. Peng, Z. Wei, C. Wan, J. Li, Z. Chen, D. Zhu, D. Baumann, H. Liu, C. S. Allen, X. Xu, *Nat. Catal.* **2020**, *3*, 762.
- [6] Z. Du, X. Chen, W. Hu, C. Chuang, S. Xie, A. Hu, W. Yan, X. Kong, X. Wu, H. Ji, *J. Am. Chem. Soc.* **2019**, *141*, 3977.
- [7] H. Pan, K. S. Han, M. H. Engelhard, R. Cao, J. Chen, J. G. Zhang, K. T. Mueller, Y. Shao, J. Liu, *Adv. Funct. Mater.* **2018**, *28*, 1707234.
- [8] Q. Pang, X. Liang, C. Y. Kwok, L. F. Nazar, *Nat. Energy* **2016**, *1*, 16132.
- [9] M. Zhang, W. Chen, L. Xue, Y. Jiao, T. Lei, J. Chu, J. Huang, C. Gong, C. Yan, Y. Yan, *Adv. Energy Mater.* **2020**, *10*, 1903008.
- [10] D. Su, D. Zhou, C. Wang, G. Wang, *Adv. Funct. Mater.* **2018**, *28*, 1800154.
- [11] S. F. Ng, M. Y. L. Lau, W. J. Ong, *Adv. Mater.* **2021**, 2008654.
- [12] X. Tao, J. Wang, C. Liu, H. Wang, H. Yao, G. Zheng, Z. W. Seh, Q. Cai, W. Li, G. Zhou, *Nat. Commun.* **2016**, *7*, 11203.
- [13] X. Liu, J. Q. Huang, Q. Zhang, L. Mai, *Adv. Mater.* **2017**, *29*, 1601759.
- [14] X. Liang, C. Y. Kwok, F. Lodi-Marzano, Q. Pang, M. Cuisinier, H. Huang, C. J. Hart, D. Houtarde, K. Kaup, H. Sommer, *Adv. Energy Mater.* **2016**, *6*, 1501636.
- [15] J. He, G. Hartmann, M. Lee, G. S. Hwang, Y. Chen, A. Manthiram, *Energy Environ. Sci.* **2019**, *12*, 344.
- [16] Z. Yuan, H.-J. Peng, T.-Z. Hou, J.-Q. Huang, C.-M. Chen, D.-W. Wang, X.-B. Cheng, F. Wei, Q. Zhang, *Nano Lett.* **2016**, *16*, 519.
- [17] Z. Sun, J. Zhang, L. Yin, G. Hu, R. Fang, H.-M. Cheng, F. Li, *Nat. Commun.* **2017**, *8*, 14627.
- [18] J. Shen, X. Xu, J. Liu, Z. Liu, F. Li, R. Hu, J. Liu, X. Hou, Y. Feng, Y. Yu, *ACS Nano* **2019**, *13*, 8986.
- [19] S. Yu, W. Cai, L. Chen, L. Song, Y. Song, *J. Energy Chem.* **2021**, *55*, 533.
- [20] S. Wang, S. Feng, J. Liang, Q. Su, F. Zhao, H. Song, M. Zheng, Q. Sun, Z. Song, X. Jia, *Adv. Energy Mater.* **2021**, *11*, 2003314.
- [21] S. Zhou, S. Yang, X. Ding, Y. Lai, H. Nie, Y. Zhang, D. Chan, H. Duan, S. Huang, Z. Yang, *ACS Nano* **2020**, *14*, 7538.
- [22] B. Yang, H. Jiang, Y. Zhou, Z. Liang, T. Zhao, Y.-C. Lu, *ACS Appl. Mater. Interfaces* **2019**, *11*, 25940.
- [23] H. Chu, J. Jung, H. Noh, S. Yuk, J. Lee, J. H. Lee, J. Baek, Y. Roh, H. Kwon, D. Choi, *Adv. Energy Mater.* **2020**, *10*, 2000493.
- [24] M. Baek, H. Shin, K. Char, J. W. Choi, *Adv. Mater.* **2020**, *32*, 2005022.
- [25] X. Gao, Y. Chen, L. Johnson, P. G. Bruce, *Nat. Mater.* **2016**, *15*, 882.
- [26] Z. Gong, R. Liu, H. Gong, G. Ye, J. Liu, J. Dong, J. Liao, M. Yan, J. Liu, K. Huang, *ACS Catal.* **2021**, *11*, 12284.
- [27] F. Wang, H. Fu, F.-X. Wang, X.-W. Zhang, P. Wang, C. Zhao, C.-C. Wang, *J. Hazard. Mater.* **2022**, *423*, 126998.
- [28] Y. Tian, X. Liu, L. Xu, D. Yuan, Y. Dou, J. Qiu, H. Li, J. Ma, Y. Wang, D. Su, *Adv. Funct. Mater.* **2021**, *31*, 2101239.
- [29] M. Kuang, J. Zhang, D. Liu, H. Tan, K. N. Dinh, L. Yang, H. Ren, W. Huang, W. Fang, J. Yao, *Adv. Energy Mater.* **2020**, *10*, 2002215.
- [30] S. Huang, Y. Meng, Y. Cao, F. Yao, Z. He, X. Wang, H. Pan, M. Wu, *Appl. Catal. B: Environ.* **2020**, *274*, 119120.
- [31] X. Yang, X. Xu, J. Wang, T. Chen, S. Wang, X. Ding, H. Chen, *Sol. RRL* **2021**, *5*, 2000442.

- [32] T. Sun, X. Zhao, B. Li, H. Shu, L. Luo, W. Xia, M. Chen, P. Zeng, X. Yang, P. Gao, *Adv. Funct. Mater.* **2021**, 2101285.
- [33] Z. Li, Q. Zhang, L. Hencz, J. Liu, P. Kaghazchi, J. Han, L. Wang, S. Zhang, *Nano Energy* **2021**, *89*, 106331.
- [34] M. Malligavathy, R. A. Kumar, C. Das, S. Asokan, D. P. Padiyan, *J. Non-Cryst. Solids* **2015**, *429*, 93.
- [35] M. Ye, J. Jia, Z. Wu, C. Qian, R. Chen, P. G. O'Brien, W. Sun, Y. Dong, G. A. Ozin, *Adv. Energy Mater.* **2017**, *7*, 1601811.
- [36] Q. Wang, S. Zhang, H. He, C. Xie, Y. Tang, C. He, M. Shao, H. Wang, *Chem. Asian J.* **2021**, *16*, 3.
- [37] T. Leichtweiss, R. A. Henning, J. Koettgen, R. M. Schmidt, B. Holländer, M. Martin, M. Wuttig, J. Janek, *J. Mater. Chem. A* **2014**, *2*, 6631.
- [38] H. Okamoto, *J. Phase Equilib. Diffus.* **2011**, *32*, 473.
- [39] C. Shen, J. Xie, M. Zhang, P. Andrei, J. P. Zheng, M. Hendrickson, E. J. Plichta, *J. Power Sources* **2019**, *414*, 412.
- [40] Z. Shen, M. Cao, Z. Zhang, J. Pu, C. Zhong, J. Li, H. Ma, F. Li, J. Zhu, F. Pan, *Adv. Funct. Mater.* **2020**, *30*, 1906661.
- [41] Z. Li, C. Zhou, J. Hua, X. Hong, C. Sun, H. W. Li, X. Xu, L. Mai, *Adv. Mater.* **2020**, *32*, 1907444.
- [42] D. Luo, Z. Zhang, G. Li, S. Cheng, S. Li, J. Li, R. Gao, M. Li, S. Sy, Y.-P. Deng, *ACS Nano* **2020**, *14*, 4849.
- [43] X. Yu, M. J. Boyer, G. S. Hwang, A. Manthiram, *Chem* **2018**, *4*, 586.
- [44] C. S. Pedersen, J. H. Chang, Y. Li, N. Pryds, J. M. Garcia Lastra, *APL Mater.* **2020**, *8*, 071108.
- [45] R. Li, D. Rao, J. Zhou, G. Wu, G. Wang, Z. Zhu, X. Han, R. Sun, H. Li, C. Wang, *Nat. Commun.* **2021**, *12*, 3102.
- [46] S. Nosé, *J. Chem. Phys.* **1984**, *81*, 511.
- [47] L. Du, Q. Wu, L. Yang, X. Wang, R. Che, Z. Lyu, W. Chen, X. Wang, Z. Hu, *Nano Energy* **2019**, *57*, 34.
- [48] C. Li, S. Qi, L. Zhu, Y. Zhao, R. Huang, Y. He, W. Ge, X. Liu, M. Zhao, L. Xu, *Nano Today* **2021**, *40*, 101246.
- [49] Y. Liu, S. Ma, L. Liu, J. Koch, M. Rosebrock, T. Li, F. Bettels, T. He, H. Pfnür, N. C. Bigall, *Adv. Funct. Mater.* **2020**, *30*, 2002462.
- [50] H. Zhang, L. K. Ono, G. Tong, Y. Liu, Y. Qi, *Nat. Commun.* **2021**, *12*, 4738.
- [51] H. Pan, J. Chen, R. Cao, V. Murugesan, N. N. Rajput, K. S. Han, K. Persson, L. Estevez, M. H. Engelhard, J.-G. Zhang, *Nat. Energy* **2017**, *2*, 813.
- [52] H. Chu, H. Noh, Y.-J. Kim, S. Yuk, J.-H. Lee, J. Lee, H. Kwack, Y. Kim, D.-K. Yang, H.-T. Kim, *Nat. Commun.* **2019**, *10*, 188.
- [53] Z. Liu, D. Hubble, P. B. Balbuena, P. P. Mukherjee, *Phys. Chem. Chem. Phys.* **2015**, *17*, 9032.
- [54] T. Yu, F. Li, C. Liu, S. Zhang, H. Xu, G. Yang, *J. Mater. Chem. A* **2017**, *5*, 9293.
- [55] Z. Li, Y. Zhou, Y. Wang, Y. C. Lu, *Adv. Energy Mater.* **2019**, *9*, 1802207.
- [56] D. Lv, J. Zheng, Q. Li, X. Xie, S. Ferrara, Z. Nie, L. B. Mehdi, N. D. Browning, J. G. Zhang, G. L. Graff, *Adv. Energy Mater.* **2015**, *5*, 1402290.
- [57] D. B. Babu, K. Ramesha, *Carbon* **2019**, *144*, 582.
- [58] J. L. Cheong, A. A. AbdelHamid, J. Y. Ying, *Nano Energy* **2019**, *66*, 104114.